

A Simple Model for Pulse Profiles from Precessing Pulsars, with Special Application to Relativistic Binary PSR B1913+16

Timothy Clifton

Department of Astrophysics, University of Oxford, Oxford OX1 3RH, UK

T.Clifton@cantab.net

Joel M. Weisberg

Department of Physics and Astronomy, Carleton College, Northfield, MN 55057

jweisber@carleton.edu

Received 2007 October 14; accepted 2008 February 4

Astrophysical Journal **679**, 687 (2008).

ABSTRACT

We study the observable pulse profiles that can be generated from precessing pulsars. A novel coordinate system is defined to aid visualization of the observing geometry. Using this system we explore the different families of profiles that can be generated by simple, circularly symmetric beam shapes. An attempt is then made to fit our model to the observations of relativistic binary PSR B1913+16. It is found that while qualitatively similar pulse profiles can be produced, this minimal model is insufficient for an accurate match to the observational data. Consequently, we confirm that the emission beam of PSR B1913+16 must deviate from circular symmetry, as first reported by Weisberg & Taylor (2002). However, the approximate fits obtained suggest that it may be sufficient to consider only minimal deviations from a circular beam in order to explain the data. We also comment on the applicability of our analysis technique to other precessing pulsars, both binary and isolated.

1. Introduction

Most pulsars spin about an axis that remains fixed in space, relative to our line of sight. However, in some cases the spin axis will precess. The free precession of an isolated pulsar due to a body asymmetry with respect to its spin axis is one such case; the general relativistic “geodetic” precession of the spin axis of a pulsar in a binary system about its orbital angular momentum vector is another (Damour & Ruffini 1974; Barker & O’Connell 1975a,b; Börner, Ehlers & Rudolph 1975; Hari Dass & Radhakrishnan 1975).

Spin precession, whatever its cause, allows our line of sight to progress across the pulsar emission beam. As this occurs, the observed pulse profile will also evolve. The detection of

such changes in pulse shape is consequently a hallmark of spin axis precession. Whilst we are forever bound to receive beamed emission from a single latitude on a non-precessing pulsar, the presence of precession, and the resulting pulse shape changes, enable us to make inferences about the two-dimensional structure of the pulsar emission beam, and the likely geometry of the system.

Secular pulse shape changes in PSR B1913+16 ascribed to geodetic precession were first reported by Weisberg, Taylor, & Romani (1989). As more data accumulated in the mid-1990s, and the signature of precession became clearer, it became possible to use the observed change in the separation of the two principal pulse components (Kramer 1998) to pick the geometrical models that best fit the observational data. The pioneering work of Kramer (1998) assumed a simple circular region emitting a conical beam of radiation from the pulsar. Using this model Kramer performed a least-squares fit on the observed pulse component separation data to find the best-fitting parameters that described the geometry of the system. Later investigations were performed by Weisberg & Taylor (2002, 2005; hereafter WT02, WT05). In these papers, the authors decomposed the pulse profile into symmetric and anti-symmetric parts and considered not only the time evolution of the peaks of the symmetric pulse profile, but also the separations of the contours of lower intensity. The profiles they obtained show that the equal intensity contours in the center of the profile appear to be moving together more quickly than those at the edge, which may even be slowly moving apart. The authors were unable to account for this strange behavior with a circular beam model; instead they generalized the shape of the emission beam to that of an ‘hourglass’ by adding two more parameters to the beam model. The parameters describing this deformed shape, and those describing the geometry of the system, were then fitted to the data to find a best model.

Our purpose here is to further investigate the observational consequences of a precessing

circular beam model. It is possible to envisage a number of different ways in which our line of sight could precess through the pulsar’s emission beam, each leading to qualitatively different observations of the evolution of the pulse profile here on Earth. We investigate the different ‘families’ of profiles that can be generated by different geometries of the pulsar. Using this analysis we take a new look at families that provide good candidates for the geometry of the geodetically precessing binary pulsar PSR B1913+16, and use them to revisit the question of whether this simple model is adequate to fit the observed data, as contested by WT02 and WT05. We also comment on the applicability of this analysis for other precessing pulsars.

2. The Model

In order to investigate the types of pulse profile variation that can be observed from a precessing pulsar, we need to make assumptions about the shape of the beam being emitted and the nature of the precession process. We will allow the emitting region to be two-dimensional - that is, we will consider an emitting *area* being projected outwards from the pulsar, rather than simply an emitting line. This will allow us to generate families of pulse profiles of the flux density observed on Earth as a function of pulse longitude and precession phase. For simplicity and clarity we will only consider emission beams that are circularly symmetric. More general beam shapes could be considered, but this would unnecessarily complicate the present study which is designed to focus on the effects of different precession geometries and beam orientations on the pulse profile. Furthermore, for the purpose of specificity, we will build our model around the assumption that the precession is induced by the presence of a binary companion, which causes the spin axis to precess about the orbital angular momentum vector. However, we emphasize that the families of pulse shape would be the same for any type of spin precession process, and it

would be straightforward to recast this model for the case of an isolated pulsar’s precession.

2.1. The Rotating Coordinate System

The coordinate system we use to model the geometry of the binary pulsar system is shown in Fig. 1. We keep the same notation as WT02 where convenient, but choose our coordinates so that the spin vector \vec{K} and orbital angular momentum vector \vec{J} of the pulsar are *stationary*. While this coordinate system, which rotates at the precession rate, may seem less natural than one in which the bulk of the Universe is stationary (up to cosmological expansion), it will prove useful for visualizing the effect of the precession. A right-handed Cartesian coordinate system $(\hat{x}, \hat{y}, \hat{z})$ is included in the figure. The \hat{z} -direction is chosen to be aligned with \vec{K} , and \hat{x} is chosen to lie in the plane defined by the vectors \vec{K} and \vec{J} .

2.1.1. Spin Axis Precession

We consider a model in which the spin vector \vec{K} , and orbital angular momentum vector \vec{J} are fixed in space. The precession of the spin vector \vec{K} about the orbital angular momentum vector¹ \vec{J} is then equivalent to rotating the rest of the Universe, including the pulsar-Earth line of sight $\hat{n}(t)$, about \vec{J} (see the dashed cone upon which $\hat{n}(t)$ precesses in Fig. 1). The phase of the precession (equivalent to the phase of the cyclical motion of $\hat{n}(t)$)

¹In fact, the spin vector precesses about the total angular momentum vector. However, here the spin vector is smaller than the orbital angular momentum vector, so the total angular momentum vector and the orbital angular momentum vector are effectively aligned.

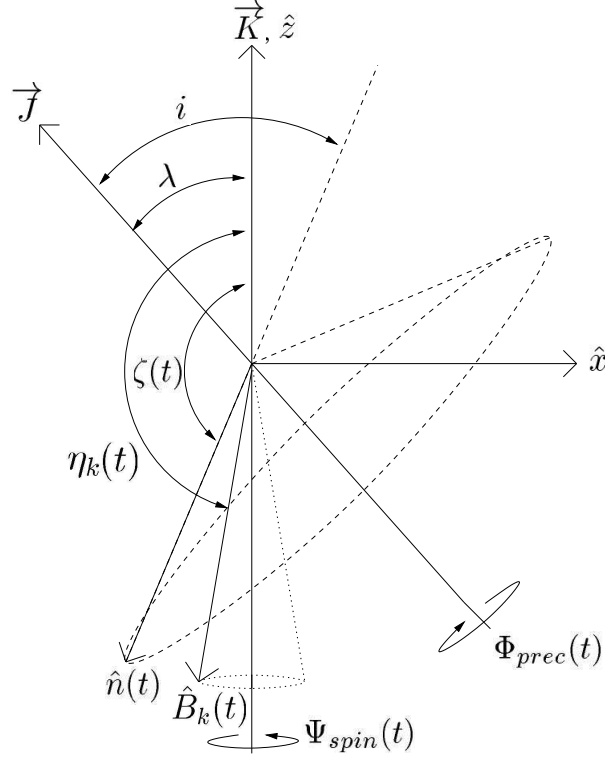


Fig. 1.— Geometry of the binary pulsar in a rotating Cartesian coordinate system $(\hat{x}, \hat{y}, \hat{z})$ fixed to the pulsar spin vector \vec{K} and orbital angular momentum vector \vec{J} . The \hat{z} -axis of the coordinate system is defined to be parallel to \vec{K} , while the \hat{x} -axis is defined to lie in the plane containing \vec{J} and \vec{K} (also the plane of the page). Dashes represent the conical trajectory of the pulsar-Earth line of sight $\hat{n}(t)$ as spin precession carries it around \vec{J} ; while dots represent the conical trajectory of a corotating beam-element vector $\hat{B}_k(t)$ as the pulsar spin carries it around $-\vec{K}$. The time-variable vectors $\hat{n}(t)$ and $\hat{B}_k(t)$ are chosen to be initially in the \hat{x} - \hat{z} plane. In accord with standard pulsar naming convention, $\zeta(t)$ is the (time-variable) spin colatitude of the pulsar-Earth line of sight. The colatitude of $\hat{B}_k(t)$ measured from \vec{K} is denoted by $\eta_k(t)$, the precession phase is $\Phi_{prec}(t)$ and the spin phase is $\Psi_{spin}(t)$. See text for additional details.

about \vec{J}) is given by $\Phi_{prec}(t)$, where

$$\Phi_{prec}(t) = \Omega_{prec} \times (t - t_0). \quad (1)$$

Here t_0 is a constant chosen so that \hat{n} lies in the x - z plane at $\Phi_{prec}(t_0) = 0$, and Ω_{prec} is the time averaged spin precession rate of the pulsar. In Fig. 1, i is the fixed (orbital) inclination angle between \vec{J} and $-\hat{n}$, λ is the fixed spin-orbit misalignment angle between \vec{K} and \vec{J} , and $\zeta(t)$ is the colatitude of the line of sight $\hat{n}(t)$ measured from spin vector \vec{K} , with $\hat{n}(t)$ describing a cone of half-angle i about \vec{J} on precession timescales.

The type of spin precession relevant to the binary pulsar PSR B1913+16 is relativistic geodetic precession. Damour & Ruffini (1974) and Barker & O’Connell (1975a,b) calculate the rate of such precession for a binary system to be

$$\Omega_{prec,geodetic} = \frac{1}{2} \left(\frac{GM_\odot}{c^3} \right)^{2/3} \left(\frac{P_b}{2\pi} \right)^{-5/3} \frac{m_c(4m_p + 3m_c)}{(1 - e^2)(m_p + m_c)^{4/3}} \quad (2)$$

where m_p and m_c are the pulsar and companion masses measured in units of the solar mass M_\odot , P_b is the orbital period and e is the eccentricity. For the binary system PSR B1913+16 $\Omega_{prec,geodetic}$ is calculated to be 1.21°yr^{-1} (WT02). [More general expressions for $\Omega_{prec,geodetic}$ in terms of the post-Newtonian parameterization can be found in Will (1993)].

2.1.2. Pulsar Spin

We define a general vector $\hat{B}_k(t)$ which corotates with the spinning pulsar at a colatitude η_k measured from \vec{K} . For our purposes, $\hat{B}_k(t)$ can represent the beamed radiation from some particular point on the emission cone. The effect of the pulsar’s rotation is for the vector $\hat{B}_k(t)$ to rotate about \vec{K} . Fig. 1 shows a corotating beam vector $\hat{B}_k(t)$; its spin about $-\vec{K}^2$ is illustrated with dotted lines. The phase of the rotation $\Psi_{spin}(t)$ is marked on

²In general, $\hat{B}_k(t)$ spins about either $\pm\vec{K}$, but for PSR B1913+16, it is closer to $-\vec{K}$.

the figure and is given by $\Psi_{spin}(t) = \omega_{spin}t$ where ω_{spin} is the pulsar spin frequency, which can be written in terms of the pulsar pulse (or spin) period P_{spin} as $\omega_{spin} = 2\pi/P_{spin}$.

3. Generating the Observed Pulse Profile

Having defined the important vectors in §2, we can now proceed to generate the observed pulse profile as a function of time.

3.1. The Line of Sight and Corotating Beam Element Vectors $\hat{n}(t)$ and $\hat{B}_k(t)$

In considering the precession of the rotating pulsar, we are interested in the motion of the pulsar-Earth line of sight $\hat{n}(t)$, and of a vector $\hat{B}_k(t)$ corotating with the pulsar that represents an emission beam element. These two vectors are the ones that sweep out cones in Fig.1. In terms of the Cartesian coordinates (x, y, z) , these vectors can be written

$$\begin{aligned} \hat{n}(t) = \begin{pmatrix} x \\ y \\ z \end{pmatrix} &= \begin{pmatrix} -\cos \lambda \sin i \cos \Phi_{prec}(t) + \sin \lambda \cos i \\ \sin i \sin \Phi_{prec}(t) \\ -\sin \lambda \sin i \cos \Phi_{prec}(t) - \cos \lambda \cos i \end{pmatrix}; \\ \hat{B}_k(t) &= \begin{pmatrix} -\sin \eta_k \cos \Psi_{spin}(t) \\ -\sin \eta_k \sin \Psi_{spin}(t) \\ \cos \eta_k \end{pmatrix}. \end{aligned} \quad (3)$$

The paths swept out by these vectors as they rotate about \vec{J} and \vec{K} , respectively, are small circles on the unit sphere centered on the pulsar. Transforming to spherical polar coordinates (θ, ϕ) on the unit sphere, where the azimuthal angle in the (x, y) -plane is $\theta \equiv \tan^{-1}(y/x)$ and the polar angle with respect to the \hat{z} axis is $\phi \equiv \cos^{-1} z$, we have

$$\hat{n}(t) = \begin{pmatrix} \theta \\ \phi \end{pmatrix} = \begin{pmatrix} -\tan^{-1} \left\{ \frac{\sin i \sin \Phi_{prec}(t)}{(\cos \lambda \sin i \cos \Phi_{prec}(t) - \sin \lambda \cos i)} \right\} \\ \cos^{-1} \{ -\cos \lambda \cos i - \sin \lambda \sin i \cos \Phi_{prec}(t) \} \end{pmatrix};$$

$$\hat{B}_k(t) = \begin{pmatrix} \Psi_{spin}(t) \\ \eta_k \end{pmatrix}. \quad (4)$$

In order to present these trajectories on the page (as we will below), it is necessary to project them from the above spherical coordinate system onto a plane with polar coordinates (r, Θ) , where the radial coordinate³ is $r \equiv \pi - \phi$ and the azimuthal angle is $\Theta \equiv \theta$. They then become

$$\begin{aligned} \hat{n}(t) = \begin{pmatrix} r \\ \Theta \end{pmatrix} &= \begin{pmatrix} \cos^{-1} \{ \cos i \cos \lambda + \cos \Phi_{prec}(t) \sin i \sin \lambda \} \\ \cot^{-1} \{ \cot i \csc \Phi_{prec}(t) \sin \lambda - \cos \lambda \cot \Phi_{prec}(t) \} \end{pmatrix}; \\ \hat{B}_k(t) &= \begin{pmatrix} \pi - \eta_k \\ \Psi_{spin}(t) \end{pmatrix}. \end{aligned} \quad (5)$$

The coordinate system $(\hat{r}, \hat{\Theta})$ is chosen such that its origin corresponds to the point at which the $-\vec{K}$ spin axis passes through the unit sphere. The small circles swept out by the corotating vector $\hat{B}_k(t)$ on the unit sphere are now circles in the plane, centered on the origin; while the small circles swept out much more slowly by the line of sight vector $\hat{n}(t)$ are non-circular closed curves (ovals).

3.2. Generating the Circular Beam from a Set of Beam Elements

So far we have calculated the geometry of a single arbitrary point $\hat{B}_k(t)$, which can be taken to be a beam element, corotating with the pulsar. This analysis can be generalized to a conical beam by intersecting a plane P_j perpendicular to the beam's axis with the unit sphere, giving a small circle C_j consisting of a *set* of $\hat{B}_k(t)$ intersecting the sphere. For our

³We choose here r to be equal to the supplement of ϕ rather than ϕ itself because the observed beam is near the $-\vec{K}$ spin pole for PSR B1913+16. It would be more natural to set $r \equiv \phi$ if the observed beam were nearer the $+\vec{K}$ spin pole.

ansatz of a circularly symmetric emitting area the contours of constant intensity will be concentric circles on the unit sphere, corotating with the pulsar. It is therefore sufficient to consider a set of concentric circles in order to model our simple circularly symmetric emitting area. This picture will be built up by first considering a single emitting circle, and then many concentric emitting circles representing the contours of constant intensity.

Since most pulsar emission models center the emission cone on the star’s magnetic axis $\hat{\mu}$ closest to the line of sight, we will also define our conal axis to be along $\hat{\mu}$. Because $\hat{\mu}$ corotates with the pulsar, its trajectory is described by the equations of a beam vector which we will call $\hat{B}_0(t)$; i.e., $\hat{\mu} \equiv \hat{B}_0(t)$. The spin colatitude of the magnetic axis, the angle between \hat{K} and $\hat{\mu}$, is called α . While our model does not depend on the beam axis coinciding with the magnetic axis, this specific choice aids in visualizing the model and in naming some of the vectors and angles with the conventional nomenclature of pulsar astrophysics.

3.2.1. A Single Circular Emission Cone

We will now generate a single infinitesimally thin (i.e., hollow), constant intensity emission cone labelled C_j by intersecting the unit sphere with a plane $P_{\mu,j}$ defined to be normal to the cone axis $\hat{\mu}$ (see Fig. 2). For mathematical simplicity, consider the moment of time when the beam axis is in the (x, z) -plane (defined by $\theta = 0$) so that its direction is given by $\hat{\mu} = \hat{x} \sin \alpha + \hat{z} \cos \alpha$. Specifying any point in the plane $P_{\mu,j}$, at this moment, uniquely determines it and the small circle C_j (the emission beam) it creates as it intersects the unit sphere. We choose this point to be on the surface of the sphere in the (x, z) -plane, where $\theta = 0$. The point is then either the beam element closest to or farthest from the spin pole $-\vec{K}$. We choose it to be the closest and label it $B_{1,j}(t)$ with a corresponding

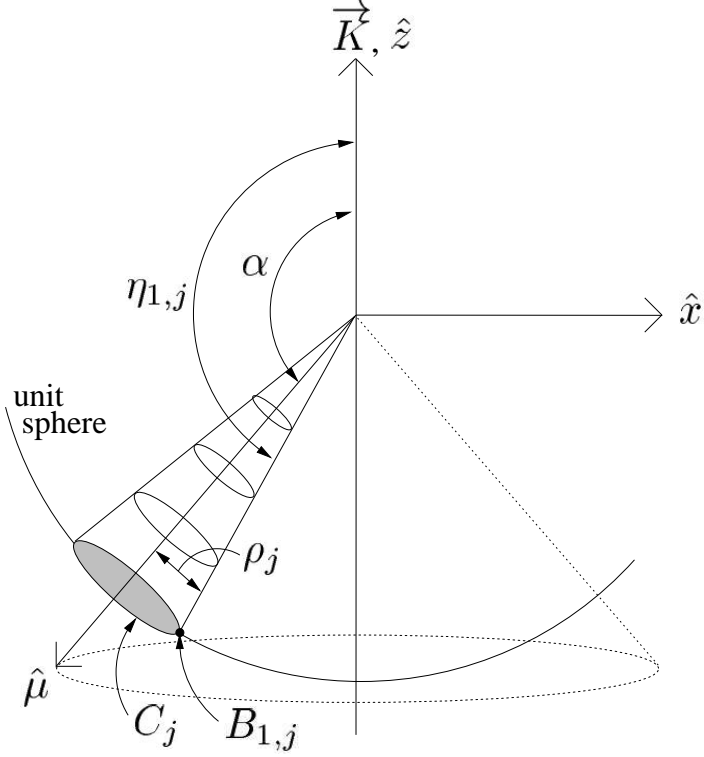


Fig. 2.— An illustration of a single circular emission cone. This figure focuses on an entire circular beam, while Fig. 1 showed only a single arbitrary element of the beam, \hat{B}_k . The coordinate system is identical to Fig. 1, with \hat{z} fixed to the pulsar spin vector \vec{K} as shown. A single hollow emission cone, C_j , centered on the vector $\hat{\mu}$ (which is also the magnetic axis in many emission models) is generated by intersecting the unit sphere with a (shaded) plane perpendicular to $\hat{\mu}$. The cone C_j is defined by the associated quantities $B_{1,j}$, $\eta_{1,j}$, and ρ_j : $B_{1,j}$ labels the point on C_j that is closest to $-\vec{K}$; $\eta_{1,j}$ is the angle between \vec{K} and the vector extending from the origin to $B_{1,j}$; and ρ_j is the angular radius of C_j . The dotted lines denote the trajectory followed by the beam axis $\hat{\mu}$ during a rotation of the pulsar. Following standard pulsar nomenclature, the angle α is the (fixed) spin colatitude of the beam axis.

colatitude⁴ $\eta_{1,j}$. Note that this small circle of emission, C_j , represents a constant intensity beam with angular radius $\rho_j = (\eta_{1,j} - \alpha)$. The equation of C_j at this moment is, in our spherical (θ, ϕ) system,

$$\sin \alpha (\cos \theta \sin \phi - \sin \eta_{1,j}) + \cos \alpha (\cos \phi - \cos \eta_{1,j}) = 0; \quad (6)$$

which, in terms of the (r, Θ) polar coordinates, becomes

$$\sin \alpha (\cos \Theta \sin r - \sin \eta_{1,j}) - \cos \alpha (\cos r + \cos \eta_{1,j}) = 0. \quad (7)$$

An observer at the end of the line of sight vector \hat{n} , with colatitude $\phi = \zeta(t)$ from \vec{K} , will see two events in quick succession as the pulsar's rotation carries the emission beam cone C_j across \hat{n} . From Eq. 6 we can see that these two events, which we can interpret as the passage of leading and trailing contours of equal intensity across the line of sight, will have the longitudinal (i.e., rotational phase) separation

$$w_j(t) = 2 \cos^{-1} \left\{ \frac{\cos \rho_j - \cos \alpha \cos \zeta(t)}{\sin \alpha \sin \zeta(t)} \right\} \quad (8)$$

where it has been assumed that \hat{n} is effectively static for the period of one rotation of the pulsar.

Eq. 8 gives $w_j(t)$ in terms of the observer's slowly precessing colatitude $\zeta(t)$. We can now determine $\zeta(t)$ as a function of the precession phase $\Phi_{prec}(t)$, which is linear in t (see Eq. 1), by recognizing that $\zeta(t)$ is just the $\hat{\phi}$ component of $\hat{n}(t)$ (see Eq. 4):

$$\cos \zeta(t) = -\cos \lambda \cos i - \sin \lambda \sin i \cos \Phi_{prec}(t). \quad (9)$$

⁴Subscript 1 here denotes the value of this quantity at its closest point to $-\vec{K}$, and does not indicate any particular value of j .

3.2.2. Building the Beam from a Set of Circular Emission Cones

In the previous section we found Eqs. 8 and 9 which give the evolution of $w_j(t)$, the leading-to-trailing longitudinal separation of a single (j^{th}) circular intensity contour C_j of the beam as a function of t . We will now generalize this notation by considering $w_j(t)$ to be the time-dependent separations of *multiple* constant intensity contours, each having angular radius ρ_j , where the $j = 1, 2, 3 \dots$ label each contour individually. By considering the time evolution of several different $w_j(t)$ simultaneously for fixed values of α , i and λ , we can build up a picture of the pulse profile received from the whole emitting cone as the system precesses. This will be done in the next section.

4. The Observable Form of the Pulse Profile

We have now developed the tools required to analyze and to visualize the problem of the different types of observed pulse profiles that can be generated as a binary pulsar undergoes spin axis precession. Our $(\hat{r}, \hat{\Theta})$ polar coordinate system centered on the spin axis is particularly convenient for this task, since any vector corotating with the pulsar at colatitude η_k (e.g., a beam element vector \hat{B}_k) will forever traverse a fixed circular trajectory of radius $(\pi - \eta_k)$ about the $-\hat{K}$ spin axis at angular velocity $\omega = \omega_{spin}$. Meanwhile, the path slowly travelled by the precessing line of sight \hat{n} , while also cyclical, will be a *deformed* circle in this coordinate system, since it is the the projection of a circular trajectory onto a lower dimensional reference plane. An observer will see a pulse at those phases of the precession cycle where the line of sight \hat{n} intersects some part of the circling beam. There are a number of ways that this can occur, leading to a number of qualitatively different pulse profiles for the observer along \hat{n} . These loci of intersection can be found in the $(\hat{r}, \hat{\Theta})$ coordinate system using Eqs. (5), the trajectories of the precessing line of sight \hat{n} and corotating beam elements \hat{B}_k .

In the following sections, we present pairs of plots displaying the precessing beam from two vantage points. First, we display the trajectories of the beam and the line of sight for particular geometries in the polar, $-\hat{K}$ -centered coordinate system. However, *terrestrial* observers will not be able to observe such a plot directly; they will only see a pulse emission profile, changing over the precession cycle. Therefore, we also present the form of the pulse profile as seen by a terrestrial observer lying along \hat{n} , as a function of precession phase. We will call this depiction the “2DPP” (two-dimensional pulse profile) to distinguish it from conventional 1-dimensional pulse intensity profiles. In what follows, we restrict ourselves to geometries appropriate for the relativistic binary PSR B1913+16, but the tools developed here can be used to visualize variations in the pulse profile of any pulsar undergoing spin precession.

4.1. The Observable Form of a Single Circular Emission Cone

To fix ideas we will first consider the observable form of a single corotating emitting cone C_1 , in $(\hat{r}, \hat{\Theta})$ space. Recall that we showed C_j in Fig. 2 with its axis $\hat{\mu}$ instantaneously “frozen” at some value of Θ . We also plotted the corotating trajectory of the beam axis $\hat{B}_0 = \hat{\mu}$. Our present purpose is to illustrate how different 2DPPs can be generated. The specific conditions required to separate the different classes will be found subsequently. We will restrict ourselves to situations producing pulse profiles that approximate those observed for the system PSR1913+16 (Weisberg, Taylor, & Romani 1989; Kramer 1998; Weisberg & Taylor 2002, 2005). Throughout the 1980’s, observations of this system showed that the pulse profile did not appear to be affected greatly by geodetic precession. To generate a relatively unchanging pulse profile during some period, it is necessary for the line of sight trajectory \hat{n} to stay at an approximately constant radial distance from the spin axis (the origin of the $(\hat{r}, \hat{\Theta})$ plane) during this time, whilst remaining inside the zone through

which the beam circulates. That is, the oval line of sight trajectory must be approximately tangent to that of the emission beam, in order to minimize precession-induced beam shape changes, in concert with the observations made in the 1980's. In the following two sections, we describe such line of sight trajectories as they approach the beam circulation zone from the outside and the inside, respectively.

4.1.1. *The Line of Sight Enters into the Beam Circulation Zone from the Outside*

For the line of sight \hat{n} to enter the beam circulation zone from the outside, we must have $i > \pi - \eta_{1,2} \sim \pi - \alpha$ (see Fig. 1). There are two qualitatively different types of such outer trajectories. Both of these situations are shown together with the resultant pulse profiles that would be observed in Figs. 3a and 3b, respectively. The first trajectory in Fig. 3a (the dot-dashed line) is chosen so that it probes only the outer region of the beam circulation zone. In this case the line of sight vector \hat{n} precesses into the outermost edge of the beam circulation zone, but never progresses very far into it before precessing out again. (Specifically, \hat{n} never crosses inside the circle swept out by the beam axis $\hat{\mu}$.) The second trajectory in Fig. 3a (the dashed line) follows much the same path but critically it precesses further into the beam circulation zone before reversing its progress. (In this case, \hat{n} *does* cross inside of the circle described by $\hat{\mu}$.) The effect of this can be clearly seen in the observed pulse profile widths w , shown as a function of precessional phase in Fig. 3b. The shallow outer trajectory, shown as a dot-dashed line, produces a 2DPP that varies with time in such a way as to produce an oval-shaped contour, whilst the more deeply penetrating dashed line produces an hourglass shape. The waist of the hourglass occurs as the line of sight approaches the *inner* edge of the emission zone, the circle traversed by $\hat{B}_{1,1}$. The best fit model found by Kramer (1998) lies somewhere between these two models, where \hat{n} progresses far enough to create a briefly stationary pulsewidth w (as

observed in the 1980's) but not far enough to show the hourglass behavior. On the other hand, the hourglass-shaped 2DPPs produced by our *circular* beam model are reminiscent of the behavior found more recently by WT02 and WT05, leading one to ask if their more complicated beam model is truly necessary.

4.1.2. *The Line of Sight Enters into the Beam Circulation Zone from the Inside*

Now consider the situation where the line of sight \hat{n} enters and exits the beam circulation zone through its *inside* edge (the one closest to the spin axis; see Fig. 4) rather than its outside edge as above. In this case, $i < \pi - \eta_{1,1} \sim \pi - \alpha$. Again, there are the oval (hourglass) 2DPP contours for trajectories that are allowed to precess slightly (deeply) into the beam circulation zone. Indeed, for the case of a single emitting cone, C_1 , the inner entry pulse profiles shown in Fig. 4b are quite similar to the outer entry case shown in Fig. 3b. We will see below that the outer/inner entry degeneracy is lifted when considering multiple emitting cones.

4.2. Building Up a Pulse Profile from a Set of Concentric Emission Cones

When considering only one infinitesimally thin emitting cone C_1 , the differences in 2DPP between the outer and inner line of sight entry cases, illustrated respectively in Figs. 3b and 4b, are difficult to appreciate. However, when we broaden our considerations to simultaneously include j concentric circles C_j (each one representing a distinct equal-intensity contour), the observed pulse profiles exhibit a more complicated and interesting behavior. We will see that the time evolution of the pulse profile is dependent not only on the trajectory of \hat{n} but also on the radius ρ_j of each particular contour C_j . Specifically, the observer at \hat{n} would see that some of the j equal-intensity contours exhibit hourglass-shaped

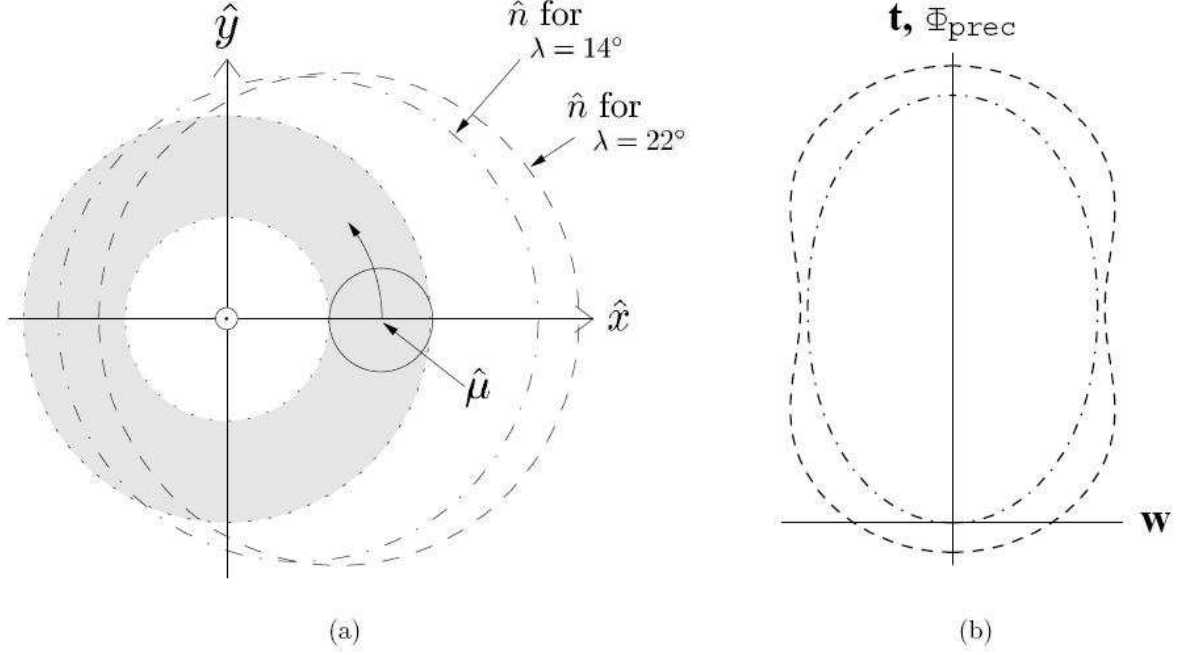


Fig. 3.— Line of sight entry points into the beam circulation zone from the *outside*, for a *single* hollow conical beam C_1 having radius $\rho_1 = 10^\circ$ and colatitude $\alpha = 150^\circ$; with orbital inclination $i = 47.2^\circ$. (a) Spin-axis centered map of beam circulation zone (shaded circular region) and precessing lines of sight \hat{n} (ovals) projected onto the $(\hat{r}, \hat{\Theta})$ and (\hat{x}, \hat{y}) plane. The beam C_1 (shown as a circle centered on $\hat{\mu}$) corotates with the pulsar, filling in the shaded zone in one spin period. The dot-dashed (dashed) oval represents the trajectory of \hat{n} for spin-orbit misalignment angle $\lambda = 14^\circ$ (22°). (b) The resulting two-dimensional pulse profile (2DPP), as observed at the end of \hat{n} , showing profile longitudinal width, w , as a function of precession phase, Φ_{prec} . (Note that Φ_{prec} is linear in time: $\Phi_{\text{prec}} = \Omega_{\text{prec}} \times (t - t_0)$). The profile width w represents the separation between two pulse components originating from the leading and trailing portions of the emission cone C_1 . Dot-dashed and dashed lines are for the same two values of λ as in (a).

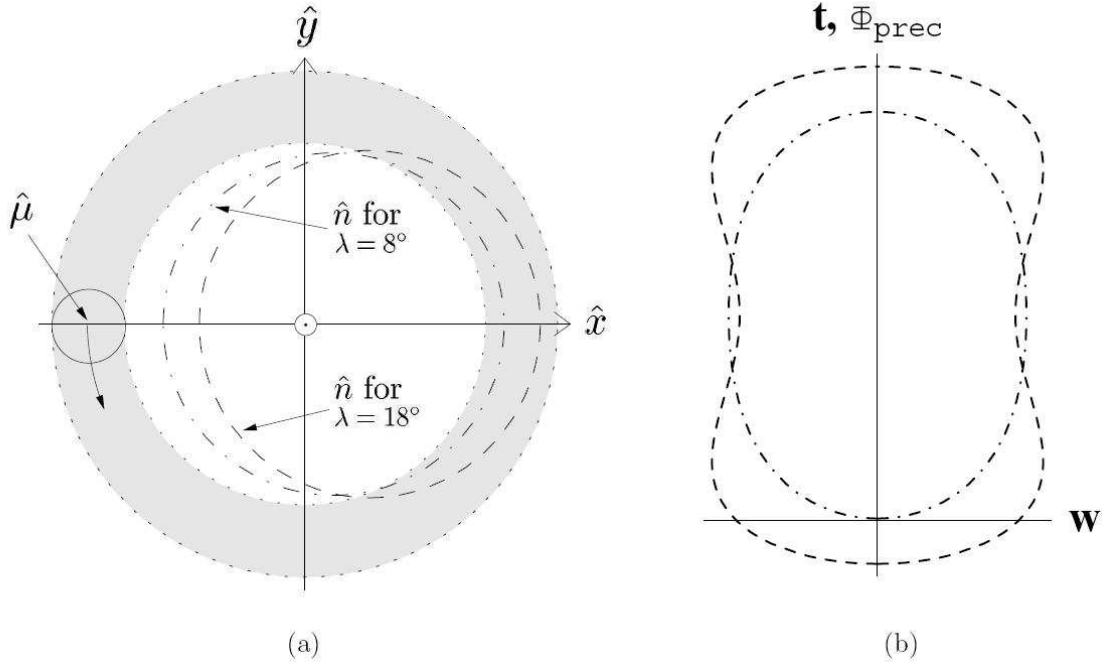


Fig. 4.— A line of sight entry into the beam circulation zone from the *inside*, for a *single* conal beam C_1 having radius $\rho_1 = 10^\circ$ and colatitude $\alpha = 120^\circ$; with orbital inclination $i = 47.2$. The dot-dashed (dashed) curves are for $\lambda = 8^\circ$ (18°). See Fig. 3 caption for more details.

2DPPs, like the dashed curves of Figs. 3b and 4b, whilst simultaneously seeing others with oval shaped contours, like the dot-dashed curves in those figures. This is particularly interesting as it appears that observations of PSR1913+16 show exactly this behavior (WT02, WT05). We will now show the qualitative difference between the *families* of 2DPP contours that are generated for the outer and inner line of sight entry cases.

Fig. 5 presents an example of a family of 2DPP contours generated by an outer line of sight entry into the beam circulation zone. Fig. 6 shows an example of an inner entry. Whilst the form of *single* contours was shown above to be qualitatively similar for inner and outer entries of similar depth, it is clear from Figs. 5 and 6 that *families* of concentric contours are quite different in the outer and inner entry cases. In Fig. 5b the outer 2DPP contours are ovals while the inner ones are hourglass-shaped. Figure 6b exhibits exactly the opposite behavior.

The best fit model of Kramer (1998) represents a shallow outer line of sight entry with⁵ $i > \pi - \alpha$, as illustrated by the dot-dashed curve in Fig. 3. Whilst Kramer’s best fit model does accurately reproduce the observations for a *single* contour of PSR B1913+16 (the contour of peak intensity, as measured by the Arecibo and Effelsberg telescopes up through the mid-1990s), it does not appear to match the observations when a whole family of concentric contours are considered⁶ (WT02, WT05). However, the simple circularly symmetric, *multiple* cone model considered here appears able to produce the same approximate shape as the latter observations (i.e, oval inner contours and hourglass-shaped outer ones (see Fig. 5)).

⁵By Kramer’s definition of α , this condition translates to $i > \alpha$.

⁶This is due to Kramer’s model belonging to our ‘outer entry’ class of models.

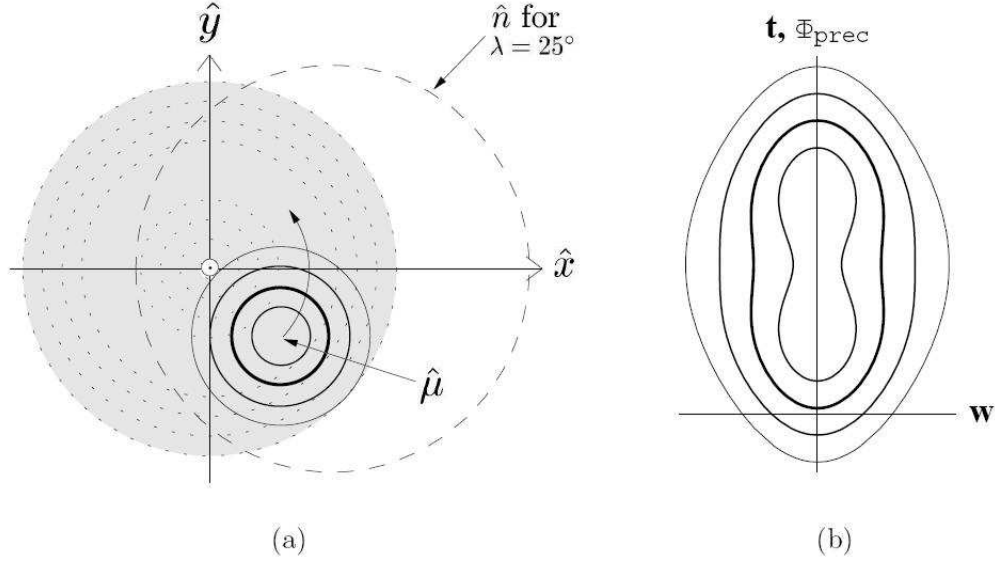


Fig. 5.— A line of sight entry into the beam circulation zone from the *outside*, for a *multiple* cone model with conal radii $\rho = 6^\circ, 10^\circ, 14^\circ$ and 18° ; and $\lambda = 25^\circ$, $\alpha = 160^\circ$ and $i = 40^\circ$. (a) Spin-axis centered map of beam circulation zone (shaded circular region); and the trajectory of the precessing line of sight vector \hat{n} (dashed line) projected onto the $(\hat{r}, \hat{\Theta})$ and (\hat{x}, \hat{y}) plane. The concentric solid circles centered on $\hat{\mu}$ depict the instantaneous position of the hollow, circular emission beams, with the line thickness representing the intensity of each one. The beams corotate with the pulsar, filling in the shaded “beam circulation zone” in one spin period. The dotted lines represent the spin trajectories of inner and outer edges of the various conical beams. (b) The resulting two-dimensional pulse profile (2DPP), as observed at the end of \hat{n} , showing profile longitudinal width w as a function of precession phase, Φ_{prec} . (Note that Φ_{prec} is linear in time: $\Phi_{\text{prec}} = \Omega_{\text{prec}} \times (t - t_0)$). Each closed curve corresponds to a separate circular emission cone. The profile width w across a particular contour represents the separation between two pulse components originating from the leading and trailing portions of each emission cone. Note that inner contours are hourglass-shaped, while outer ones are oval. See Fig. 3 caption for more details.

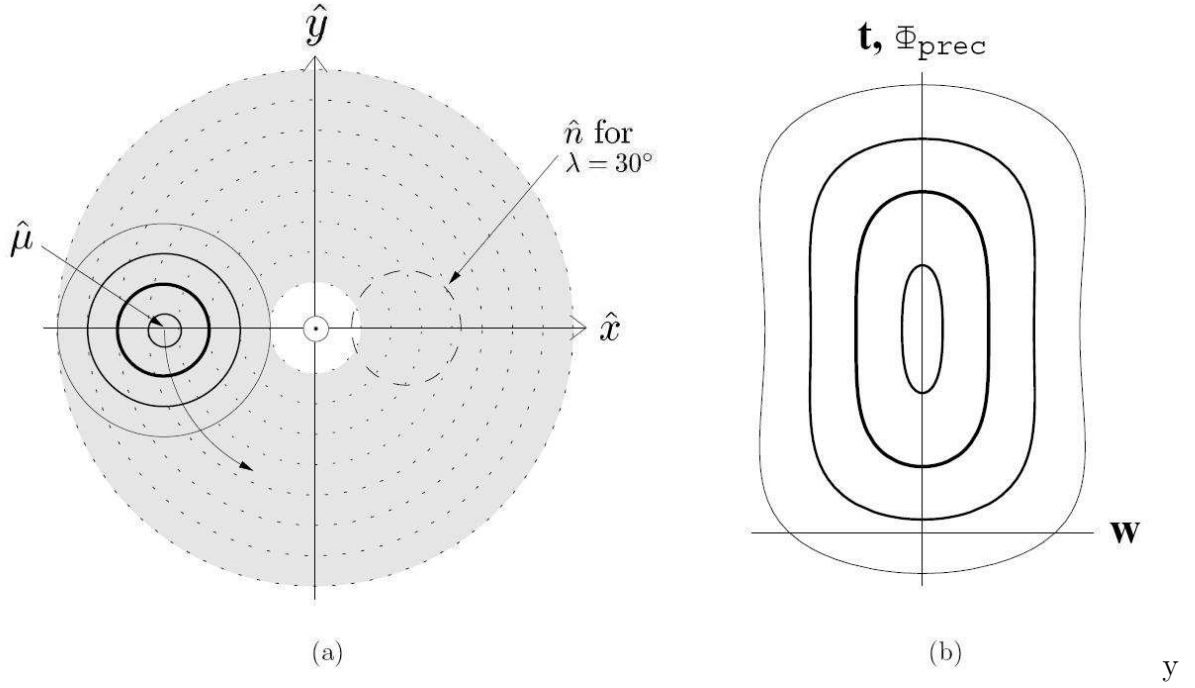


Fig. 6.— A line of sight entry into the beam circulation zone from the *inside*, for a *multiple* cone model with conal radii $\rho = 5^\circ, 15^\circ, 25^\circ$ and 35° ; and $\lambda = 30^\circ$, $\alpha = 130^\circ$ and $i = 18^\circ$. Note that the 2DPP shown in (b) resemble those of PSR B1913+16 (WT02, WT05), with inner ovals and outer hourglasses. See the captions of Figs. 5 and 3 for more details.

4.3. Conditions for Oval- and Hourglass-shaped Two-dimensional Pulse Profiles

It was seen in the previous section that it is possible to generate both oval- and hourglass-shaped 2DPPs from a circularly symmetric emitting region. We will now derive the specific conditions necessary to produce both oval and hourglass shapes together in the same two-dimensional pulse profile.

To find the precession phases Φ_{prec} at which the pulsewidth w_j of beam j is unchanging we must find the point at which

$$\frac{dw_j}{d\Phi_{prec}} = 0 \quad (10)$$

for a smooth function $w_j(\Phi_{prec})$.⁷ This condition occurs when

$$\sin \Phi_{prec} (\cot \alpha + \cos \rho_j \csc \alpha (\cos i \cos \lambda + \cos \Phi_{prec} \sin i \sin \lambda)) = 0. \quad (11)$$

For an oval-shaped 2DPP, this expression will vanish only when $\sin \Phi_{prec} = 0$; whereas an hourglass profile will have this quantity vanish two extra times when

$$\cos \Phi_{prec} = -\cot i \cot \lambda - \cos \alpha \csc i \csc \lambda \sec \rho_j. \quad (12)$$

The condition that the profile be hourglass-shaped is then the condition that the right hand side of the above equation lie between -1 and 1 . This is satisfied if ρ_j lies in the range

$$\cos(i + \lambda) < -\cos \alpha \sec \rho_j < \cos(i - \lambda) \quad (13)$$

if $\sin i > 0$, as it is for PSR B1913+16. For a specified intensity contour and binary geometry it is now straightforward to see if a 2DPP contour will be an oval or an hourglass.

⁷In terms of Figs. [3b-6b], we are finding the phases at which the j^{th} 2DPP contour is vertical.

Furthermore, Equation (13) can be used to establish whether a family of contours will produce hourglass shapes for its smallest or largest radii - that is, whether its pulse profile looks like Fig. 5 or Fig. 6. To see this we first note that ρ must lie within the range 0 to $\pi/2$, in order that the emitting region should cover less than the entire surface of the pulsar. The quantity $\cos \alpha \sec \rho$ then increases in magnitude as ρ becomes larger (for fixed α)⁸.

4.3.1. *Small Hourglasses*

We first consider the conditions necessary to produce hourglass-shaped *inner* 2DPP contours; i.e, those that are hourglasses as $\rho \rightarrow 0$, so that $\sec \rho \rightarrow 1$. Taking this limit of Eq. 13 we find that if α lies in the range

$$\cos(i + \lambda) < -\cos \alpha < \cos(i - \lambda), \quad (14)$$

then the innermost profile contours will be hourglass-shaped. Now, if $(-\cos \alpha)$ satisfies Eq. 14, and is also sufficiently close to $\cos(i - \lambda)$, then the contours with larger ρ will be ovals even while the inner ones remain hourglass-shaped.

4.3.2. *Small Ovals*

For the smallest 2DPP contours to be oval-shaped, α must satisfy either

$$-\cos \alpha < \cos(i + \lambda) \quad (15)$$

or

$$-\cos \alpha > \cos(i - \lambda). \quad (16)$$

⁸We restrict ourselves here to considering $\alpha > \pi/2$, as appropriate for PSR B1913+16.

The first of these small-radius oval-contour conditions allows for the possibility of larger radii simultaneously producing hourglass-shaped contours, and is a necessary condition to generate a profile of the form shown in Fig. 6. The second of the above bounds signifies situations in which all of the contours produce ovals.

5. Confrontation with the PSR B1913+16 Data

Having presented a way of visualizing the effects of precession, and having investigated some of the pulse profiles that can be achieved from a simple circularly symmetric emitting region, we will now confront our ideas with observational data. This will allow us to consider the degree to which deviations from this simplest model are required in order to explain the observations of PSR B1913+16. By finding the best fitting parameters for this model, we will also have found plausible starting points about which more complicated, future studies can focus.

5.1. Data Acquisition and Preliminary Analyses

All data for this study were collected at $\lambda \sim 21$ cm at Arecibo Observatory. Taylor & Weisberg (1989) present descriptions of the pulsar observing systems employed. The details of the process leading to a final “session-average” profile for each of twenty-three two-week observing sessions from 1981 to 2003 are given in WT02. Those authors and WT05 analyzed the same data set studied here.

The data exhibit the following general features. The double-peaked pulse profile exhibits a $\sim 1\%/yr$ decline in the ratio of leading to trailing peak intensity, as first discovered by Weisberg, Taylor, & Romani (1989). Until the mid-1990s, no other changes were detected, indicating that the \sim middle of a hollow conical beam was precessing across

the observer’s line of sight. The intensity ratio change was ascribed to locally “patchy” structure in the conical beam precessing across the line of sight. Kramer (1998) was the first to discover a narrowing of the separation between the two principal pulse component peaks, indicating that the center of the beam was finally precessing away from the line of sight.

All subsequent observations indicate that the profile narrowing continued, but with some interesting twists. The 2DPPs of WT02 and WT05 show that whilst the profile peaks moved together and the saddle region between them filled in, the outermost intensity contours did not converge over time and may have even diverged. It is our intention to use the new understanding delineated in §4 to search for possible circular beam solutions that could account for these observations.

5.2. Model Fits

The preliminary stages of this investigation follow the procedures of WT02 and WT05. Each session-average profile was split into even and odd parts, and subsequent analyses focused only on the even parts, under the assumption that the odd parts represented local, “patchy” structure not relevant to overall beam modelling. The pulsewidth w was then determined for each of fourteen intensity levels in all of the 23 session-average even profiles.

We then diverge from the procedures of WT02 and WT05 by fitting these data to our circularly symmetric model, rather than to their elongated beam model. We fix the sine of the orbital inclination, $\sin i$, at 0.734 [from the timing measurements of Taylor & Weisberg (1989)], and fit for four parameters: The colatitude of the magnetic axis α , the spin-orbit misalignment angle λ (see Fig. 1), the precession epoch T_0 and the overall scale factor s . [See WT02 for further discussion of these parameters.] Kramer (1998) fitted for quantities

similar to these parameters with his single contour model, and data on the separation between the profile peaks only. While the fitting process alone cannot distinguish between four degenerate solutions, the earlier work of these authors shows that one of the four is favored for other reasons. In what follows, we will focus only on this one, which in all cases has $i = 47^\circ 20'$.

5.2.1. *Fitting to the Late Precession Phase*

Let us first consider focusing the fit on the part of the two-dimensional pulse profile immediately before the pulsar beam precesses entirely out of view (i.e., at late precession phases). In this case, it can be seen immediately that geometries in which the precessing line of sight vector, \hat{n} , enters and exits the emission beam on the *outside* (as in Fig. 5b) are not good candidates to explain the observations. Conversely, the late-precession-phase 2DPP generated from the line of sight entering and exiting the emission beam from the *inside*, shown in Fig. 6b, match the observations much better. With these 2DPPs we have the inner contours converging while the outer ones remain approximately stationary, in keeping with the observations of PSR1913+16. There is also the possibility of achieving a period shortly before this in which *all* the contours remain \sim stationary, as was observed by Weisberg, Taylor, & Romani (1989). Such a period of stationarity is achieved by making the outer contours only mildly hourglass shaped, so that they appear as almost “pill” shaped. We display our attempts to find a fit in this “late precession phase” scenario in Fig. 7. We find an approximate match when $\alpha = 123^\circ 7'$ and $\lambda = 14^\circ 5'$. However, as indicated by the systematic deviations of data from the model illustrated in the figure, and quantified by a large χ^2 , the fit is not particularly good. In fact, this particular configuration does not appear as a stable solution of the fitting program.

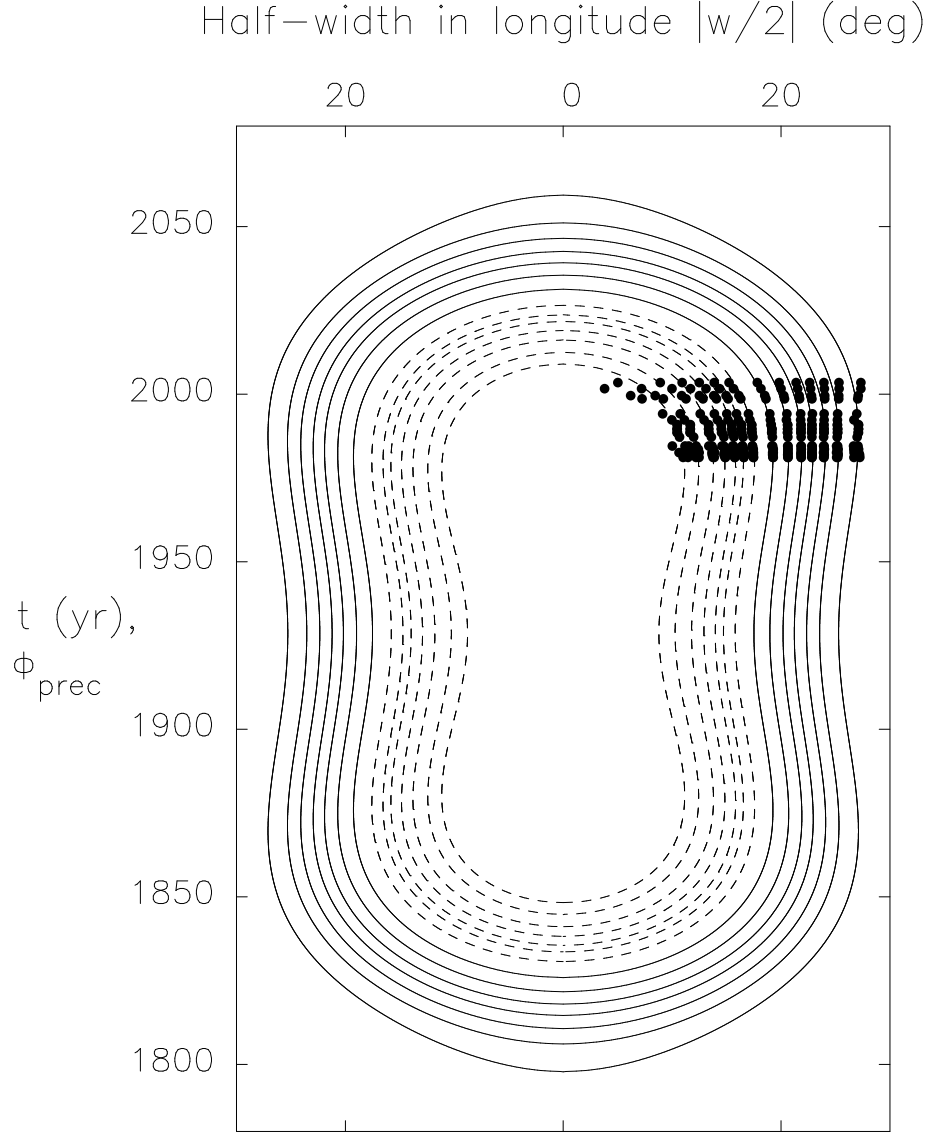


Fig. 7.— Late precession-phase fit. Fitting of the two-dimensional pulsewidth data of WT02 and WT05 to late precession phases of a model with $\alpha = 123^\circ.7$ and $\lambda = 14^\circ.5$. Each equal-intensity contour results from emission from a circularly symmetric conical beam. The intensity rises from one inner dashed contour to the next outer one; and then declines as one moves outwards among the solid contours. The vertical axis is calibrated in years, but can also be considered to be precessional phase since Φ_{prec} is linear in time. See text for additional details.

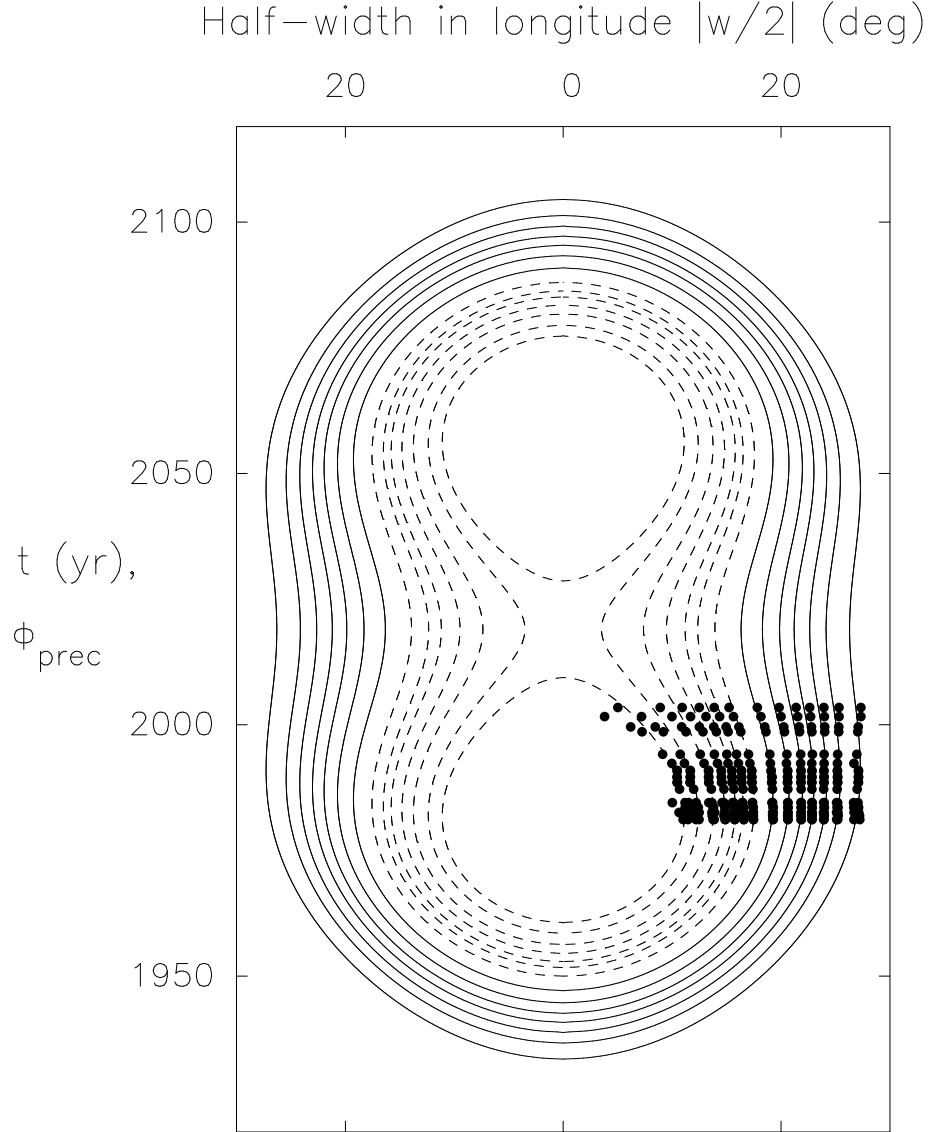


Fig. 8.— “Pre-waist” fit to 2DPPs. In this case, $\alpha = 142^\circ.8$ and $\lambda = 17^\circ.2$. Each equal-intensity contour results from emission from a circularly symmetric conical beam. See Fig. 7 and text for additional details.

5.2.2. *Fitting to the Pre-waist Precession Phase*

A second place at which to attempt a fit is near the ‘waist’ of the model 2DPP hourglass (i.e., near the middle phases of the precession cycle). In this case it is the profiles generated just *before* the midpoint of an *outer* line of sight precession cycle (see Fig. 5b) that best match the observed “inner-in” and “outer-out” contours; whilst the *inner* entry/exit 2DPP (Fig. 6b) display the incorrect behavior near these precession phases. Unfortunately, the recently observed convergence of inner contours requires such strong hourglass shapes that it is difficult to produce the required period of stationarity with this class of fit. We display our attempt to find a match in this “pre-waist” scenario in Fig. 8. We find an approximate fit with $\alpha = 142^\circ 8$ and $\lambda = 17^\circ 2$. Again, however, the fit is poor.

5.3. Discussion

Clearly these two results are not convincing enough to offer a complete explanation of the observed pulse profile from PSR1913+16 by themselves; deviations from this minimal model, such as those considered by WT02, should be considered in order to find a better fit. However, the results of this study do show us where in parameter space we can start future searches with more complicated beam shapes. By searching in the vicinity of our approximate fits, we expect that the observed pulse profiles may be explained with only minimal deviations from this maximally symmetric model.

A number of other pulsars exhibit long-term pulse profile changes that may be precession-induced, and which could thus benefit from the analysis techniques developed here. The candidates can be divided into two classes: First, binary pulsars like B1913+16 that are expected to undergo geodetic precession due to relativistic spin-orbit coupling; and second, isolated pulsars undergoing free precession caused by a body asymmetry.

Among the binary pulsars, B1913+16 currently has the most detailed and longest duration pulse shape measurements. Precession-induced pulse shape changes have also been detected in B1534+12 (Stairs et al. 2004), J1141-6545 (Hotan et al. 2005), J1906+0746 (Lorimer et al. 2006; Kasian et al. 2007), and J0737-3039B (Burgay et al. 2005). However, with the exception of the last pulsar, the trends have principally been roughly linear in time⁹. The final listed object is a member of a complicated double pulsar system, where magnetospheric interactions between the two stars are operating along with orbital and spin axis precession. Hence our model will yield no unique insights into these systems, at least until data are accumulated across a significant portion of the precession cycles.

Among the isolated pulsars showing pulse shape changes, most sources again seem to reveal long-term quasi-linear trends rather than periodic behavior. [See Weisberg et al (2007) for a review.] The most promising object is B1828-11 (Stairs et al. 2000, 2003), which shows periodic pulse shape changes on timescales of 10^{2-3} days. However, its signature exhibits a double-narrowing, a feature that is difficult to reproduce with a model of the type considered here. This suggests that B1828-11 manifests significant deviations from the highly symmetric configurations we have been considering.

6. Conclusions

We have investigated the possible pulse profiles that can be generated from a precessing pulsar which emits a simple circularly symmetric beam. We have found that a coordinate system fixed to the spin and orbital angular momentum vectors provides a useful means of visualizing the precession process and its observable consequences. We showed that a

⁹Recent progress indicates that this may not be the case with J1141-6545 (Kramer, private communication 2007).

variety of different two-dimensional pulse profiles (2DPP) can be generated from one or more *circular* beams, including profiles where the contours of constant intensity can appear as either ovals or hourglass shapes. Furthermore, we showed that it is possible to create 2DPP which are a combination of ovals and hourglasses, with the hourglass behaviour occurring at either large or small pulse widths depending on the geometry of the system.

This work has direct application to the determination of the geometry of binary systems undergoing spin precession, such as PSR 1913+16. Best fit models have previously been constructed for this system. Kramer (1998) found a best fit circular model for a single intensity contour. This model, whilst accurately modelling the peak of the profile, does not appear to produce a family of contours which fits the observational data of WT02 and WT05, while simultaneously maintaining the assumption of a circularly symmetric emitting region. Subsequent studies by WT02 and WT05 show that by giving up circular symmetry (specifically by positing an hourglass-shaped beam), it is possible to reproduce a family of contours that fits the observations well.

The results found here show that simple circularly symmetric emitting regions can generate pulse profiles which have the same qualitative form as the observational data of WT02 and WT05 - oval shaped inner contours and outer contours which come together at a later time, and are possibly even hourglass shaped. A more detailed investigation, however, has shown that this simple model is not sufficient to fit the observations completely. Nevertheless, the approximate fits we have found suggest that only minimal deviations from a perfectly circular beam may be sufficient to explain the data.

The requirement of deviations from circular symmetry should not come as a complete surprise, as we know the full pulse profile contains an asymmetric component, that cannot be easily accounted for with a circular beam. We expect the inclusion of the anti-symmetric component in future analyses should give important information about the detailed shape

of the beam.

We have shown that it is not necessary to deform the emission beam to be the same shape as the observed pulse profile, in order to produce (at least qualitatively) the required shapes. Furthermore, this investigation has shown the most likely places to start looking for fits with more complicated beam shapes, if only minimal deviations from the circular model are desired.

We expect that there will be a great many ways in which to deform the beam shape so as to produce better fits to the data. For example, one may consider circular contours of constant intensity that are not centered on exactly the same point; or, one may wish to deform each of the circles by squashing and stretching them in various ways. We expect that it will be a matter of some difficulty to show which deviations are really the most probable, but expect that it will be useful to be guided by Ockham’s razor, and consider the most minimal deviations to be the most likely.

Of course, future observations will be of great use in determining the true parameters of PSR 1913+16: Different models predict that the pulsar will precess in and out of our line of sight in different periods of time. (Compare for example, the future behavior of the pulsar as illustrated in Fig. 7 *versus* Fig. 8.) As we continue to build up a more complete picture of the two-dimensional pulse profile, it will be a considerably easier task to find the true geometry of the system.

We have also surveyed the observations of possibly precession-induced pulse shape changes in other pulsars. Most of these observations are not yet sufficiently detailed to benefit from our analysis technique. As more data are gathered in the future, these procedures will prove useful.

Acknowledgements

We would like to thank J. Barrow and M. Kramer for helpful discussions, and S. Vigeland for assistance with programming and visualization. TC acknowledges the support of the Lindemann trust. JMW has been supported by NSF Grant AST 0406832. Arecibo Observatory is operated by Cornell University under cooperative agreement with the NSF.

REFERENCES

- Barker, B. M., & O’Connell, R. F. 1975, *Phys. Rev. D*, 12, 329
- Barker, B. M., & O’Connell, R. F. 1975, *ApJ*, 199, L25
- Börner, G., Ehlers, J., & Rudolph, E. 1975, *A&A*, 44, 417
- Burgay, M., et al. 2005, *ApJ*, 624, L113
- Damour, T., & Ruffini, R. 1974, *Academie des Sciences Paris Comptes Rendus Serie Sciences Mathematiques*, 279, 971
- Hari Dass, N. D., & Radhakrishnan, V. 1975, *Astrophys. Lett.*, 16, 135
- Hotan, A. W., Bailes, M., & Ord, S. M. 2005, *ApJ*, 624, 906
- Kasian, L. E., & PALFA consortium. 2007, *ArXiv e-prints*, 711, arXiv:0711.2690
- Kramer, M., 1998, *ApJ*, 509, 856
- Kramer, M., private communication 2007
- Lorimer, D. R., et al. 2006, *ApJ*, 640, 428
- Stairs, I. H., Lyne, A. G., & Shemar, S. L. 2000, *Nature*, 406, 484
- Stairs, I. H., Athanasiadis, D., Kramer, M., & Lyne, A. G. 2003, *Radio Pulsars*, ASP Conf. Ser. 302, Ed. M. Bailes, D. J. Nice, & S. E. Thorsett. San Francisco: ASP, 249
- Stairs, I. H., Thorsett, S. E., & Arzoumanian, Z. 2004, *Physical Review Letters*, 93, 141101
- Taylor, J. H. & Weisberg, J. M. 1989, *ApJ*, 345, 434
- Weisberg, J. M., Romani, R. W., & Taylor, J. H. 1989, *ApJ*, 347, 1030

Weisberg, J. M. & Taylor, J.H. 2002, ApJ, 576, 942 (WT02)

Weisberg, J. M., & Taylor, J. H. 2005, Binary Radio Pulsars, ASP Conf. Ser. 328, Ed.

F. A. Rasio & I. H. Stairs. San Francisco: ASP, 25 (WT05). E-print available at
<http://arxiv.org/abs/astro-ph/0407149>

Weisberg, J. M., et al, 2007, astro-ph/07xxxxx

Will, C. M. 1993, Theory and Experiment in Gravitational Physics, Cambridge: Cambridge
U. Press.